Experimental and Numerical Investigation of Aerothermal Characteristics of Hypersonic Intermediate Experimental Vehicle

Article *in* Journal of Spacecraft and Rockets · April 2011

DOI: 10.2514/1.48331

CITATIONS
16

READS
593

5 authors, including:

Pietro Roncioni
CIRA Centro Italiano Ricerche Aerospaziali
56 PUBLICATIONS **528** CITATIONS
SEE PROFILE

Giuliano Ranuzzi
Agenzia Spaziale Italiana
45 PUBLICATIONS **285** CITATIONS
SEE PROFILE

Marco Marini
CIRA Centro Italiano Ricerche Aerospaziali
140 PUBLICATIONS **1,297** CITATIONS
SEE PROFILE

Emmanuel Cosson
Airbus Defense and Space
13 PUBLICATIONS **40** CITATIONS
SEE PROFILE

JOURNAL OF SPACECRAFT AND ROCKETS
Vol. 48, No. 2, March–April 2011

Experimental and Numerical Investigation of Aerothermal Characteristics of Hypersonic Intermediate Experimental Vehicle

P. Roncioni,* G. Ranuzzi,† and M. Marini‡
Italian Aerospace Research Center, 81043 Capua, Italy
S. Paris§
von Kármán Institute for Fluid Dynamics, 1640 Rhode St. Genèse, Belgium
E. Cosson¶
Astrium Space Transportation, 78133 Les Mureaux, France
and
T. Walloschek**
ESA/ESTEC, 2200 AG Noordwijk ZH, The Netherlands

DOI: 10.2514/1.48331

The main results of the aerothermodynamic hypersonic characterization of the intermediate experimental vehicle, by means of both computational fluid dynamics simulations and wind-tunnel measurements, have been reported and analyzed in this work, developed in the frame of ESA Future Launcher Preparatory Program. A test campaign has been carried out at the von Kármán Institute Free Piston Longshot wind tunnel in a cold hypersonic regime. The numerical simulations, rebuilding the von Kármán Institute wind-tunnel conditions, have been performed by the Italian Aerospace Research Center, the goal being to support the procedure of extrapolation-to-flight of the measurements and the general aerothermal characterization. A detailed comparison of all measured and predicted hypersonic relevant phenomena and aerothermodynamic parameters, such as surface pressure and heat flux, is reported in the paper, together with a detailed description of the configuration, freestream conditions, and model attitude effects. The reproducibility of flight conditions in the von Kármán Institute Longshot test campaign is qualitatively very good, both in terms of flow features and surface properties as indicated by wind-tunnel numerical simulations. The comparisons of numerical and experimental results indicate a good agreement in terms of external flow structure, i.e., bow shock, shock layer, expansion at the junction on windward side, shock-wave boundary-layer interaction in the flap area, and multiple-shock interaction above the flap. Sideslip, angle-of-attack, and flap-deflection effects are correctly reproduced by computational fluid dynamics in terms of pressure coefficient and heat flux.

Nomenclature

C_p	=	pressure coefficient
h	=	altitude, km
k	=	transition tripping device height, mm
L	=	vehicle length, m
M	=	Mach number
P	=	pressure, pa
q	=	convective heat flux, kW/m^2
Re	=	Reynolds number
T	=	temperature, k
X	=	distance along vehicle forebody running from nose, m
Y	=	spanwise vehicle coordinate, m
α	=	angle of attack, deg
β	=	angle of side slip, deg
δ	=	surface control deflection angle, deg
ε	=	emissivity coefficient

Subscripts

a	=	aileron
e	=	elevon
flap	=	body flap
L	=	reference length
left	=	left body flap
right	=	right body flap
sp	=	stagnation point
0	=	reservoir conditions
∞	=	freestream conditions

Presented at the Sixth European Symposium on Aerothermodynamics for Space Vehicles, Versailles, France, 3–6 November 2008; received 30 November 2009; revision received 20 November 2010; accepted for publication 24 November 2010.

*Ph.D. Research Engineer, Aerospace Propulsion and Reacting Flows Unit; p.roncioni@cira.it.
†Ph.D. Research Engineer, Aerospace Propulsion and Reacting Flows Unit; g.ranuzzi@cira.it.
‡Ph.D. Research Engineer, Aerospace Propulsion and Reacting Flows Unit; m.marini@cira.it.
§Research Engineer, Aeronautics and Aerospace Department; paris@vki.ac.be.
¶Intermediate Experimental Vehicle Project Manager, Astrium ST Competence Center; emmanuel.cosson@astrium.eads.net.
**Intermediate Experimental Vehicle Functional, AIV and Operations Engineer, LAU-SN; thomas.walloschek@esa.int.

I. Introduction

THE general objective of the intermediate experimental vehicle (IXV) project, developed in the framework of the ESA (European Space Agency) Future Launcher Preparatory Program, is to improve European capabilities in the strategic field of atmospheric reentry for space transportation, exploration, and scientific applications [1]. In particular the main aim of the work reported in this paper is the aerothermal characterization of the IXV vehicle by

means both computational fluid dynamics (CFD) and experimental measurements.

Atmospheric glided reentry is one the main key technologies for future space vehicle applications and several studies on experimental concepts and improvements of enabling technologies have been undertaken in recent years by ESA (ARD), France (Pre-X), Germany (Phoenix), and Italy (USV), in order to consolidate their worldwide position in this strategic field [2]. Both on-ground and in-flight tests have been scheduled and performed aimed at obtaining a good level of both reentry technologies maturation and reentry mastering at system level.

The vehicle chosen for the multipurpose reentry mission has been conceived starting from the French vehicle pre-X developed by the French space agency Centre Nationale d'Étude Spatiale, that is, a "lifting body" controlled by flaps and jets [1]. A feasibility study has been done during phase A followed by detailed activities performed during the subsequent phases [3]. In particular, the purpose of the present work is to give a more detailed aerothermodynamic analysis, both experimentally and numerically, concurrently with the progress of the project and in order to better understand the complex phenomenology governing the vehicle reentry along the glided descend trajectory.

One of the key technologies in the design of a hypersonic reentry vehicle is the aerothermodynamic that can support and address both aeroshape consolidation and mission analysis [3]. In particular the minimizing of the heat fluxes to the windward part of the vehicle (nose cap) and control surfaces (flaps) is one of the main goal of the IXV design process. An optimized flap configuration can allow reducing the necessary trimming deflection angles and, consequently, the flap peak heating. Moreover, validation and update of on-ground tools [wind tunnels (WTs) and CFD codes] can be obtained by means of in-flight experimentation.

The von Kármán Institute (VKI) was in charge of an experimental test campaign for the definition of the aerothermal database in the cold hypersonic regime. The test campaign has been carried out at the VKI Free Piston Longshot WT characterized by a test section (freestream) Mach number between 14 and 15. More precisely, the purpose was to determine the surface heat fluxes to the windward side of the model (including the sides) and the deflected flaps, but also to the base region and to the nose, by means of local measurements. As the Longshot WT allows testing at high-unit Reynolds number ($Re = 2.5 \times 10^6$–20×10^6 m^{-1}), the laminar-to-turbulent transition and the laminar/transitional/turbulent shock wave boundary layer interaction on the deflected body flaps were investigated. Surface pressure measurements were also performed for correlations assessment issues. This WT test campaign explored the angle-of-attack domain, the sideslip domain, the flap-deflection domain and the whole Reynolds number range allowable for the facility. In particular, the test campaign was carried out with three test conditions identified as "low-," "medium-," and "high"-Reynolds number. A boundary layer transition tripping device was installed for the runs devoted to the turbulence effects study (forced transition). Schlieren movies and qualitative infrared thermography analysis were performed to support the data analysis.

Numerical activities have been carried out by the Italian Aerospace Research Center (CIRA). In particular, the numerical rebuilding of the VKI Longshot WT tests (performing numerical simulations in WT conditions) has been performed to support the extrapolation-to-flight procedure. Laminar, transitional and fully turbulent flows have been computed, with air modeled as an ideal gas, for the cold WT tests' numerical rebuilding. Numerical simulations have been performed also to verify the WT settings before experimental measurements campaigns. The analysis has been performed by using the CIRA code H3NS [4] that solves the Reynolds-averaged Navier–Stokes equations on multiblock structured grids in the frame of a finite volume cell centered approach. A two-equation compressible k-ε turbulence model [5] has been used for eddy viscosity calculation while the laminar-to-turbulence transition has been imposed at the body-flap hinge line. Bow shock grid adaptation (by means of Mach isosurface grid generation process) and carbuncle phenomenon reduction methods have been necessary to obtain high-quality CFD results [6]. The numerical code has been widely used in the past and validated by means of comparisons with both WT and in-flight data [5].

The comparison of the experimental and the numerical results has provided an interesting assessment of the suitability of some modeling assumptions (e.g., grid resolution, turbulence modeling, etc.), thus suggesting proper guidelines for the ground-to-flight extrapolation rules. Specific care has been devoted to critical phenomena on the model like the shock wave boundary layer interaction and shock–shock interactions on the flaps, and the effect of the laminar-to-turbulence transition.

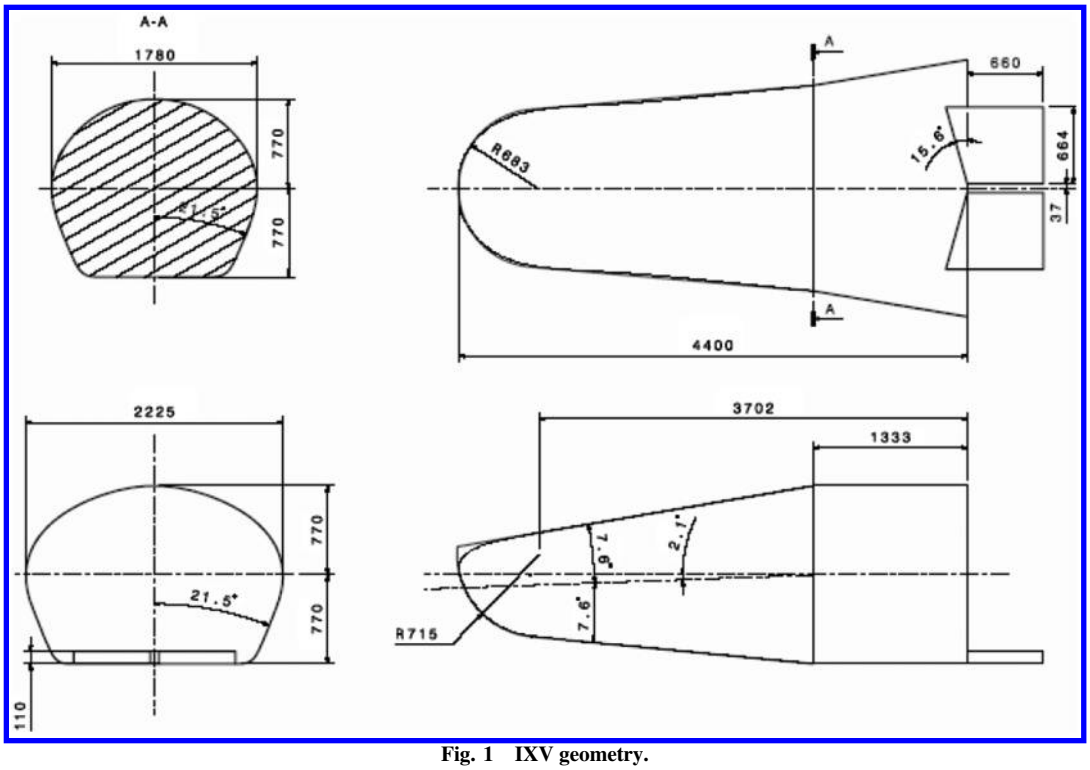

Fig. 1 IXV geometry.

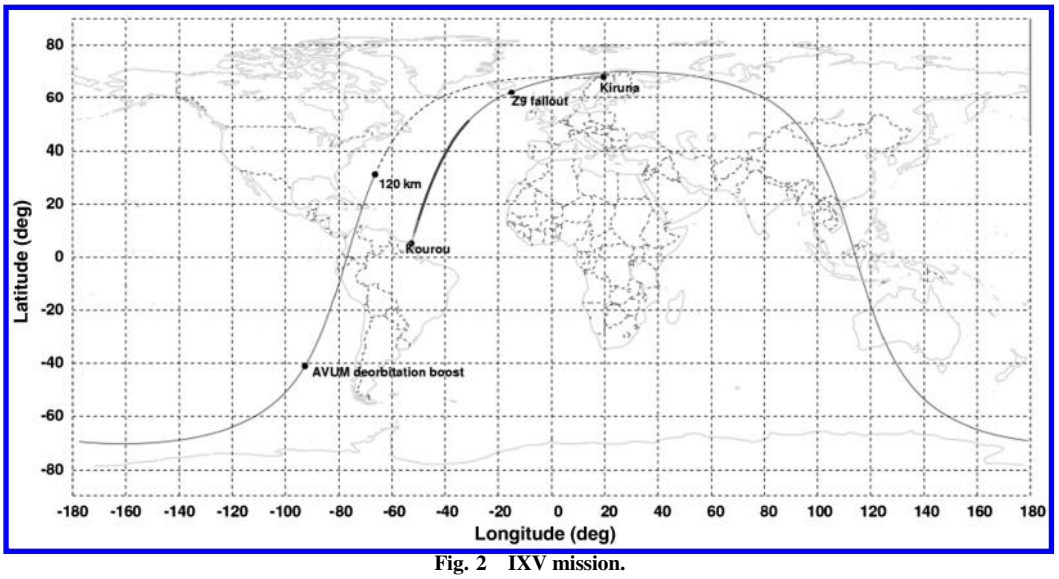

Fig. 2 IXV mission.

II. Intermediate Experimental Vehicle and Mission Description

A. Vehicle Description

The IXV reentry vehicle is, from a general point of view, a 4.4 m long and 2.2 m wide slender body configuration with a flat windward, a curved leeward and a complex three-dimensional nose, the equivalent radius of which is nearly 1.0 m for the stagnation point at an attitude of 45°. The vehicle has a lift to drag ratio (L/D) of about of 0.7 and performs a hypersonic guided reentry controlled by means of a couple of active body flaps and jets. The body flaps are tilted (the hinge line of each body flap is not orthogonal to the symmetry plane) in order to allow both longitudinal and lateral/directional control (Fig. 1). The total mass is about 1.5 Mg. The center of mass is located at $X = 2.552$ m, $Y = 0$ m, $Z = -0.11$ m with respect a body axis reference frame starting from the nose.

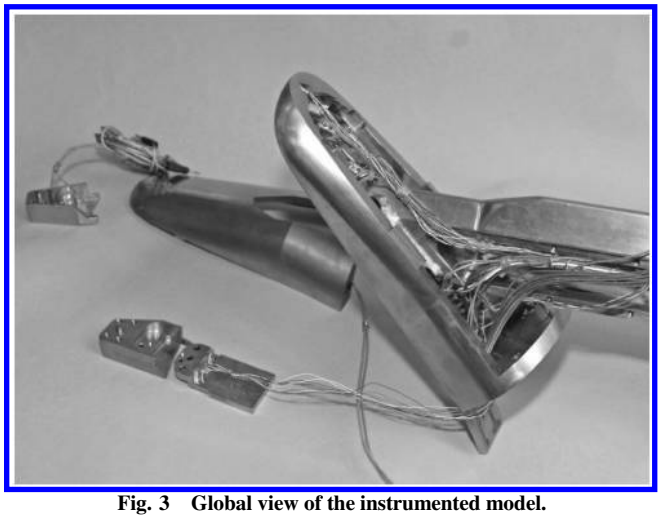

Fig. 3 Global view of the instrumented model.

B. Mission Description

The IXV vehicle's baseline mission [1] has been conceived by using the Italian rocket VEGA as launcher (Fig. 2). The reference mission plans a launch from Kourou (French Guiana) into an orbit with a 70 deg inclination, followed by a landing in the North European Aerospace Test Range at Kiruna (Sweden). Backup schemes leading to a sea landing are also being considered. VEGA's upper stage will fire above the Pacific Ocean away the coast of Chile to trigger reentry. Then, IXV will begin the reentry phase at 120 km above the Atlantic Ocean, a speed of 7.7 km/s and a path angle of 1.19 deg below the horizontal. A combination of moving aerodynamic control surfaces and thrusters will be used to control the reentry trajectory that will lasts about 20 min from hypersonic speeds, at 120 km altitude, to Mach 2.0, while traveling along a surface distance of 7500 km. A large amount of data to verify the performance of several critical reentry technologies will be gathered. IXV will then be slowed from Mach 2 by a set of parachutes and will land by means of airbags [1].

III. Experimental Activities

A. Intermediate Experimental Vehicle Model

For the WT IXV model the scale was chosen so that the reference length was 200 mm (scale 1/22) so all the reference lengths of the WT model can obtained properly scaling the full vehicle dimensions. The model is equipped with pressure transducers and thermocouples. The thermal product of the material has to be as close as possible to the one of the thermocouple, so that the wall can be considered as semi-infinite and the heat flux can be calculated. The usual candidate used for this purpose is a stainless steel: X17U4. All the pieces of the model are made of this material. A detailed view of the model inside instrumentations is shown in Fig. 3 while Fig. 4 shows the

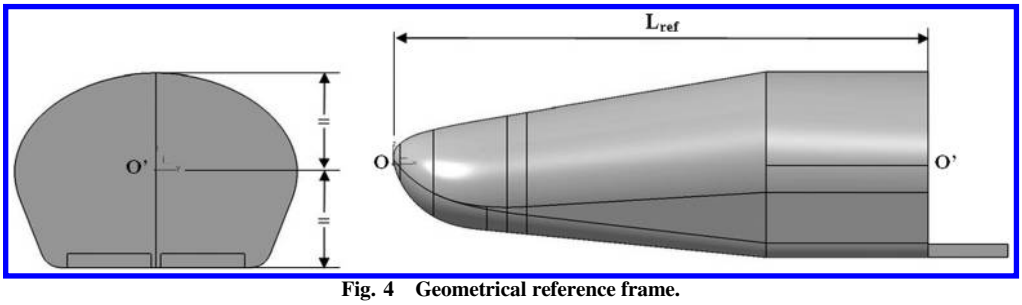

Fig. 4 Geometrical reference frame.

Fig. 5 General view of the model.

geometrical reference frame used for the layout of pressure and thermocouple sensors. The X and Z axis are located in the symmetry plane of the vehicle. In particular: the X axis is perpendicular to the aft body of the vehicle and is oriented positively backward; the Z axis is perpendicular to the X axis and is oriented positively towards the leeward side of the vehicle; the Y axis completes this axis system and is therefore oriented to the right side of the vehicle when viewed from the back to the front (pilot convention); the origin O of the geometrical reference frame is located in the symmetry plane. The distance between O and O' is equal to L_{ref}; O' being the point located in the rear base plane and in the symmetry plane halfway between the windward and the leeward sides of the vehicle. Figure 5 shows a general view of the model.

The body is the main piece on which everything is attached. The support of flap and the flap itself are fixed inside the body to avoid any disturbance on the windward side. For the same reason, the limit between the body and its cover was chosen as high as possible. An opening is made on the top of the model cover to allow for the passage of the support and the cables. The effective radius of the nose is given in the Table 1. It is used for the calculation of the normalized heat flux.

The thickness of the flap being very small (5 mm), special thermocouples were used on one flap. These 10 thermocouples are short and wires go out perpendicularly to the axes to save more height. Cavities are made in the flaps for the passage of all the wiring without any disturbance on each side. These cavities were closed by araldite. The other flap is equipped with two pressure transducers.

The tripping element is composed of sand with the correct particle size glued on the model thanks to paint. The height of the tripping element is defined following a transition criterion adapted to the distributed roughness and the computation of the boundary layer properties. Among the transition criteria available in literature, the Reshotko criterion (see [7,8]) was selected since it can be applied for distributed roughness and provides usually good results for lifting bodies [9]. Figure 6 shows the Reshotko criterion applied to the IXV vehicle for the three different test conditions of the VKI Longshot test campaign. The formulation is given by the following equation:

Table 1 Effective nose radius

α	R_{eff}, mm
35	48.441
40	48.050
45	47.648
50	47.735

$$Re_{\theta,\text{tr}} = 180(k/\theta)^{-1}(2Tw/Te)^{1.27} \quad (1)$$

with k = the size of the roughness, θ = momentum thickness, Te = temperature at edge of the boundary layer, Tw = wall temperature, $Re_{\theta,\text{tr}}$ = Reynolds number based on the momentum thickness at location of the transition.

The distributed roughness was glued approximately between 17 and 25% from the nose (see Fig. 7) that correspond to 0.034 and 0.050 m in the model reference frame (the bumps of Fig. 6 correspond the geometrical discontinuity at joining of the two windward flat zones). In this region, the criterion (k) shows that elements higher than 0.12 mm will trig the transition whatever the test conditions are. Therefore, elements 0.15 mm high were glued in order to be sure to have the transition in any case. Unfortunately for the test at low-Reynolds number, these elements were not able to produce a transition. As a consequence, it was decided to replace them by other elements 0.4 mm high.

The model is equipped with 36 thermocouples located on the left side of the model and 9 pressure transducers on the right side, as reported in Table 2.

All the axes of the pressure taps are normal to the external shape of the model. The pressure transducers have a hole diameter of 0.8 mm. For the thermocouple, the axes are normal when possible but can be slightly inclined (± 15 deg); in fact the one-dimensional heat flux hypothesis can allow a little inclination. The thermocouples being mounted flush to the wall, they do not produce any discontinuity. The thermocouples necessitate of a hole diameter of 1.55 or 1.90 mm.

The pressure sensors used in this model are all absolute miniaturized pressure transducers from Kulite (XCQ093). The pressure range varies from 5 to 50 PSI depending on the location on the model. Flush mounted coaxial thermocouples have been used to measure the transient surface temperature along the IXV model in the Longshot facility. The used thermocouples are of type "E" which consists of a material pairing of chromel/constantan with a sensitivity of about 68 μV/°C, and a response time in the range of microseconds.

B. Longshot Wind Tunnel

The VKI Longshot WT is a heavy piston gun tunnel (Fig. 8). The piston is pushed by a driver gas along a 27-m-long and 7.5-cm-diam tube in order to compress the driven gas to a pressure up to 4000 bar. The driver gas, usually nitrogen at a pressure between 300 and 1000 bar and room temperature, is contained in a 12.5-cm-diam tube 6 m long. The initial pressure of the gas in the driven tube can vary from 1 to 15 bar, and its temperature is at room temperature. The piston, weighing between 1.5 to 9 kg, is maintained by a diaphragm made in aluminum at the end of the driver tube. When that diaphragm is broken, the piston is released and is accelerated to a speed of the order of 600 m/s.

By taking into account these uncertainties on the test conditions, the global errors on the pressure coefficient and on the Stanton were computed (see Table 3). The measurements needed for calculation of the pressure coefficients and the Stanton numbers are link together. Using the classical formulation for the uncertainty produces overestimation. The uncertainty was computed by using random flow properties and measurement within the uncertainty defined before.

The test gas can be either nitrogen or carbon dioxide. The pressure increases in the reservoir up to 4000 bars with a temperature less than 2500 K which yields high-Reynolds numbers. Then, the gas expands through a contoured nozzle, characterized by a throat diameter of 6.45 mm and an exit section diameter of 420 mm (thus yielding $A/A^* = 4240$), up to Mach 15. Uniform flow is maintained for about 20 ms. The model is located at the exit of the nozzle. It is supported by a sting through a positioning mechanism with 6 degrees of freedom. Optical access allows schlieren movies to be performed.

C. Test Conditions

The test campaign was carried out with three test conditions named, respectively, low, medium and high Reynolds number using nitrogen as test gas. The purpose of the test campaign has been to

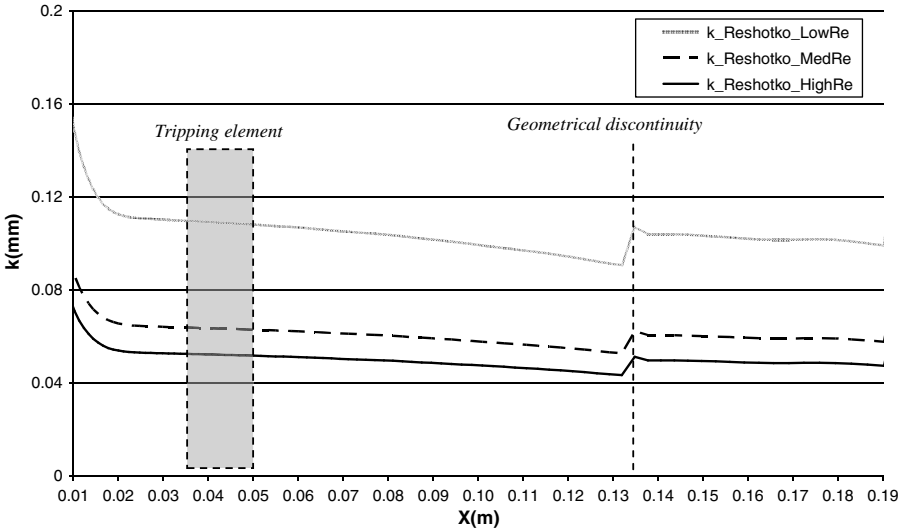

Fig. 6 Height (k) of the tripping device from Reshotko criterion.

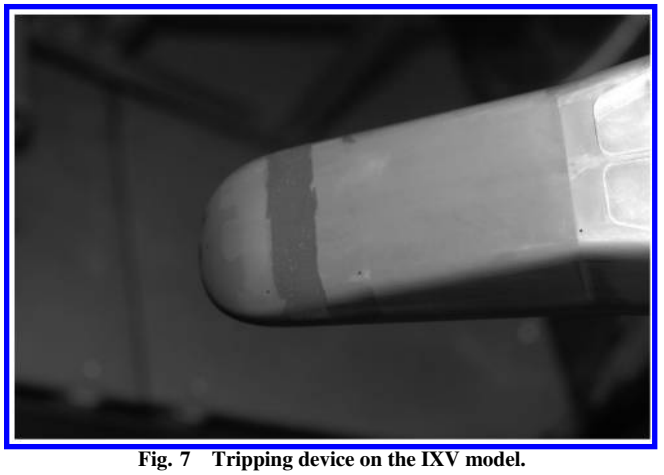

Fig. 7 Tripping device on the IXV model.

Table 2 Location of the instrumentation

Surface	Left side, thermocouples	Right side, pressure transducers
Nose region	4	2
Windward side	12	4
Leeward symmetric plane	2	——
Lateral side	5	——
Flaps	10	2
Base	3	1

Table 3 Uncertainty on the heat flux and pressure coefficient

Quantity	Uncertainty
Cp	±7%
St	±13%
$St^* Re^{0.5}$	±10%

measure the heat flux on the model in laminar, transitional and turbulent flow assumption, then the test conditions were selected to this purpose. Table 4 gives the main flow properties of these three test conditions. Reynolds number is based on the IXV model reference length $L = 200$ mm and on a viscosity calculated by means of the Keyes Law ($T < 100$ K).

Note that in the Table P_{sp} and q_{sp} are, respectively, the pitot pressure and stagnation point heat flux measured by a 25.4-mm-diam hemispherical reference probe located at 20 mm from the nozzle exit section, and at a radial position 110 mm from the centerline, this in order to avoid any interference with the IXV model. The measured heat flux q_{sp} is compared with the value obtained by means the Fay–Riddell formulation in an iterative procedure used for the settings of WT reservoir conditions as reported in Fig. 9.

IV. Numerical Activities

A. Computational Fluid Dynamics Methodology

The numerical code used to carry out the aerothermodynamic analysis of the IXV vehicle is the CIRA code H3NS that solves the Reynolds-averaged Navier–Stokes equations in a density-based block-structured finite volume approach with a cell centered, flux difference splitting second-order essentially-not-oscillatory-like upwind scheme for the convective terms (Pandolfi–Borrelli scheme; see [4]). Viscous fluxes are computed with a classical centered scheme. Time integration is performed by employing an explicit multistage Runge–Kutta algorithm coupled with an implicit evaluation of source terms of the species and vibration energy production (the terms are evaluated at $t + \Delta t/2$). The H3NS code is available in both sequential and parallel version. Working gas is air that can be properly modeled in the hypothesis of ideal gas, equilibrium gas and thermochemical non equilibrium gas (In this work only ideal gas results are presented). Different two-equation k-ε turbulence models are available in H3NS for eddy viscosity calculation. Present simulations have been performed by using the k-ε turbulence model with compressibility effects corrections [6], while laminar-to-turbulence transition has been imposed across surface lines, i.e., in present applications the transition front coincides with the body-flap hinge line. In the H3NS code the thermochemical equilibrium of air is computed by means of

Table 4 Test conditions

ID	$P0$, Pa	T_0, K	P_{sp}, Pa	q_{sp}, kW/m^2	M_∞	$Re_{\infty,L}$	p_∞, Pa	T_∞, K
Low Re	$5.99 \cdot 10^7$	1550	35,981	923.2	14.0	$1.37 \cdot 10^6$	142.2	43.2
Medium Re	$7.46 \cdot 10^7$	1405	45,195	907.0	14.2	$2.03 \cdot 10^6$	173.4	38.2
High Re	$1.04 \cdot 10^8$	1466	61,305	1153.0	14.4	$2.58 \cdot 10^6$	228.8	39.6

Table 5 IXV reentry flight and WT conditions (Reynolds number based on vehicle length *L*)

M_∞	$Re_{\infty,L}$	h, km	p_∞, Pa	T_∞, K	Condition
10.0	$6.79 \cdot 10^5$	52.1	61.19	267.8	Flight, transHL, turb, RG-Eq.
≈14.0	$1.34–2.67 \cdot 10^6$	——	——	——	VKI Long Shot, lam, transHL, turb, PG
15.0	$4.86 \cdot 10^5$	58.7	26.30	250.6	Flight, transHL, turb, Eq., RG-Neq.
17.7	$2.68 \cdot 10^5$	64.6	11.51	234.2	Flight, transHL, turb, RG-Eq.

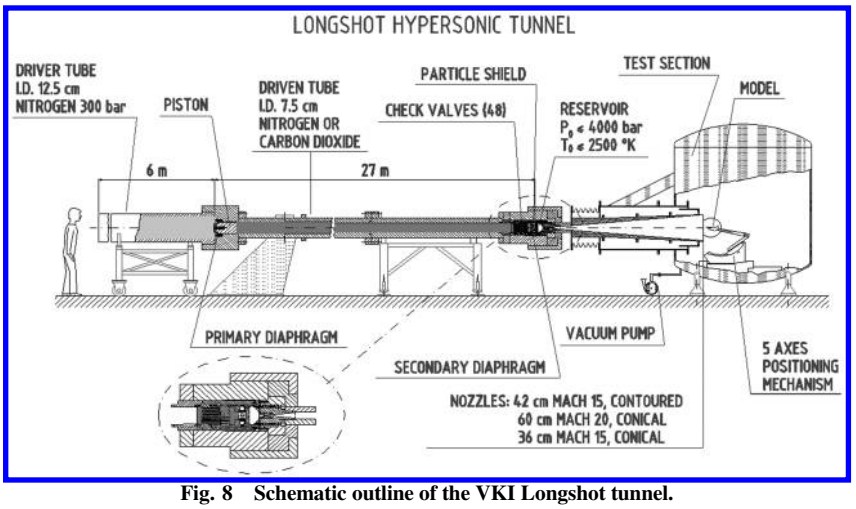

Fig. 8 Schematic outline of the VKI Longshot tunnel.

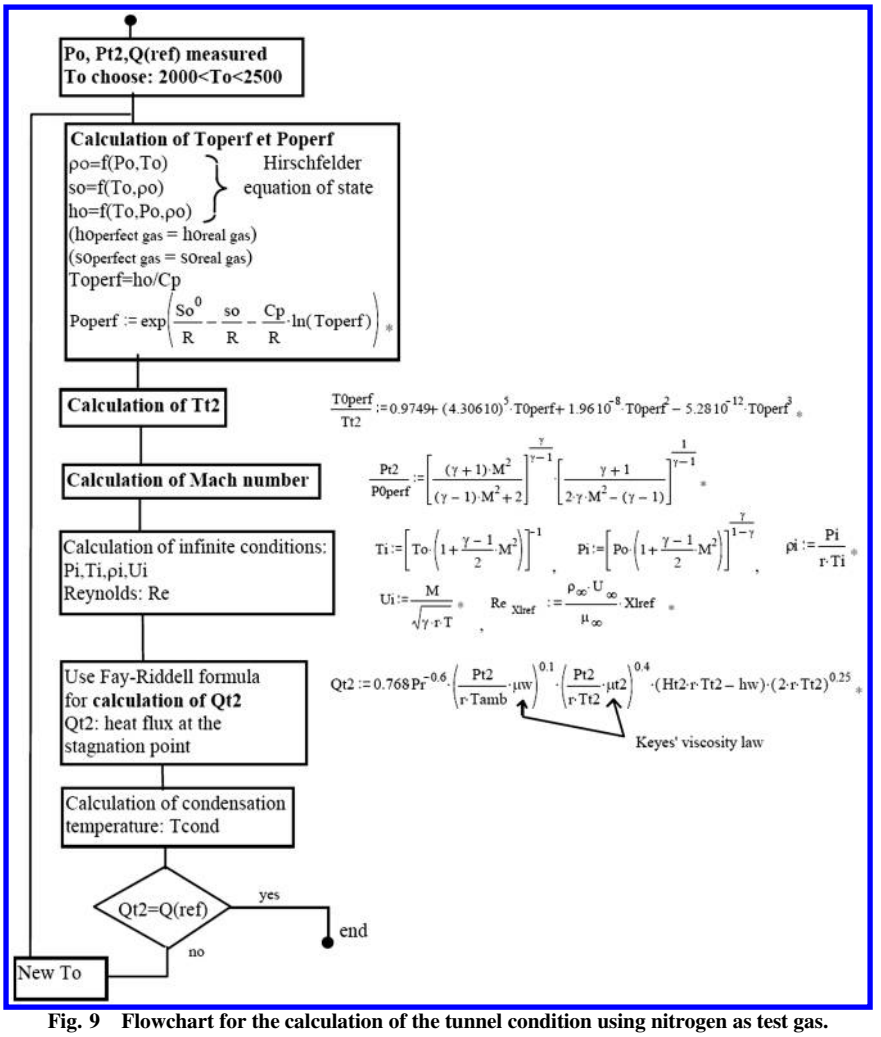

Fig. 9 Flowchart for the calculation of the tunnel condition using nitrogen as test gas.

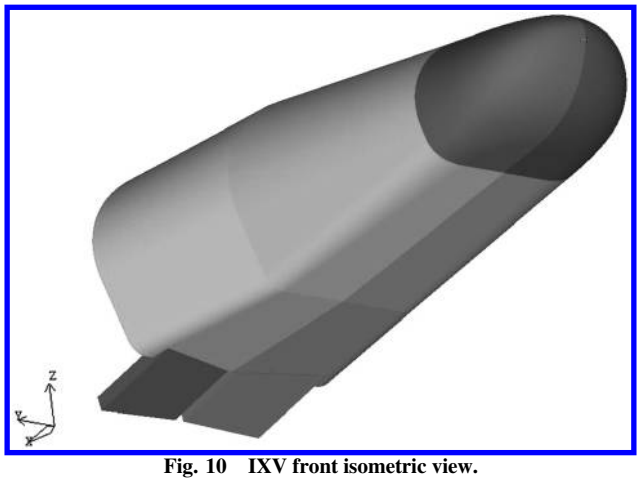

Fig. 10 IXV front isometric view.

correlation formulas of thermodynamic (enthalpy, temperature and speed of sound) properties taken from [10]. Concerning transport properties (viscosity, thermal conductivity) the curve fits have been taken from [11]. The pure nitrogen VKI Longhsot nozzle simulations have been performed by assuming a real gas behavior (dissociation is not activated due to too-low temperatures for N_2), and modelling vibration for N_2. The energy exchange between translational and vibrational modes is modeled with the classical Landau–Teller nonequilibrium equation [12], with relaxation times taken from Millikan–White theory modified by Park [13].

B. Computational Fluid Dynamics Activities

Since the end of 2006, CIRA has been in charge to conduct numerical simulations aimed to study the IXV vehicle's aerothermodynamics both in-flight (phases B_1 and B_2 at $M_\infty = 10.0, 15.0, 17.7$) and WT (VKI Longshot, $M_\infty = 14$, phase B_2) conditions. A matrix of input parameters for CFD simulations is reported in Table 5, where "RG-Eq." stands for thermochemical equilibrium real gas, "RG-Neq." for thermochemical nonequilibrium real gas, "PG" for perfect gas, "lam" for laminar flow regime, "transHL" for transition imposed at body-flap hinge line, and "turb" for fully turbulent regime. Reynolds number is based on vehicle length L, that is equal to 4.4 m for flight configuration and 0.2 m for WT model (that is scaled down by 1:22).

The IXV reentry vehicle is, from a general point of view, a 4.4 m long slender body configuration which performs a hypersonic guided reentry controlled by means of a couple of active body flaps (see Fig. 10) and a reaction control system.

Three geometric configurations have been used to carry out numerical simulations: half-body for longitudinal symmetric cases, symmetric full-body to account for sideslip effects and asymmetric full-body for longitudinal cases with different left and right flap deflection.

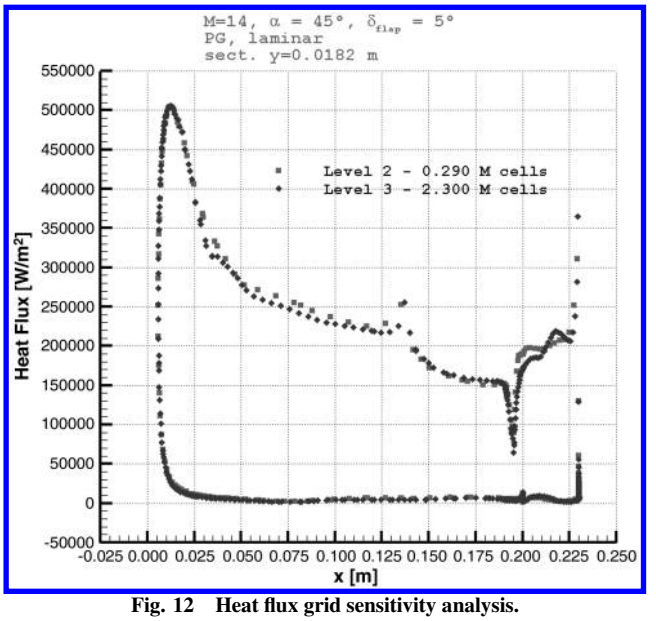

Fig. 12 Heat flux grid sensitivity analysis.

Several grids have been generated, and for each simulation a different bow shock fitting has been necessary. An example of the block decomposition is reported in Fig. 11, that shows clearly the surface and symmetry plane grid, and the topology of base and flap regions. The number of computational cells for the half-body configuration is about 2.3 million, distributed in 118 different blocks.

The analysis afforded in the initial assessment phase aimed at evaluating the sensitivity of numerical results to both the physical modeling (inviscid, laminar, turbulent) and grid refinement, and the selected numerical prediction strategy (physical modeling and number of cells) resulted in a compromise between accuracy of results and hardware availability. A rapid grid convergence has been obtained for the global aerodynamic coefficients (and pressure distributions also): low-CPU-time-demanding numerical simulations (0.3/0.4 million cells) could be used if interested in this goal only. Figure 12 shows the grid sensitivity analysis for the heat flux distribution that seems at a good grid convergence along all the selected section except for the first part of the flap zone where a difference of about 7% can be found. A third grid, definitively showing the grid convergence reaching, has not been used due to reduced time and CPU resources available. Anyway it has to be said that the use of the 2.3 m cells grid gives reliable global aerodynamic coefficients and acceptable heat flux and temperature distributions, above all considering that the design of thermal protection systems is afforded in very conservative way.

The complex phenomena characterizing the IXV vehicle flowfield (strong bow shock, shock–shock interaction, shock-wave boundary-layer interaction, base flow, flow spillage through the gap between the flaps, huge expansions) make the numerical simulations very

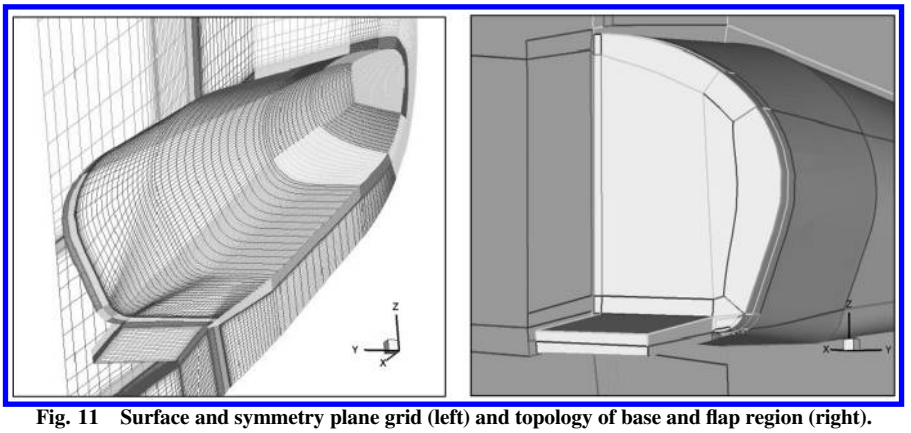

Fig. 11 Surface and symmetry plane grid (left) and topology of base and flap region (right).

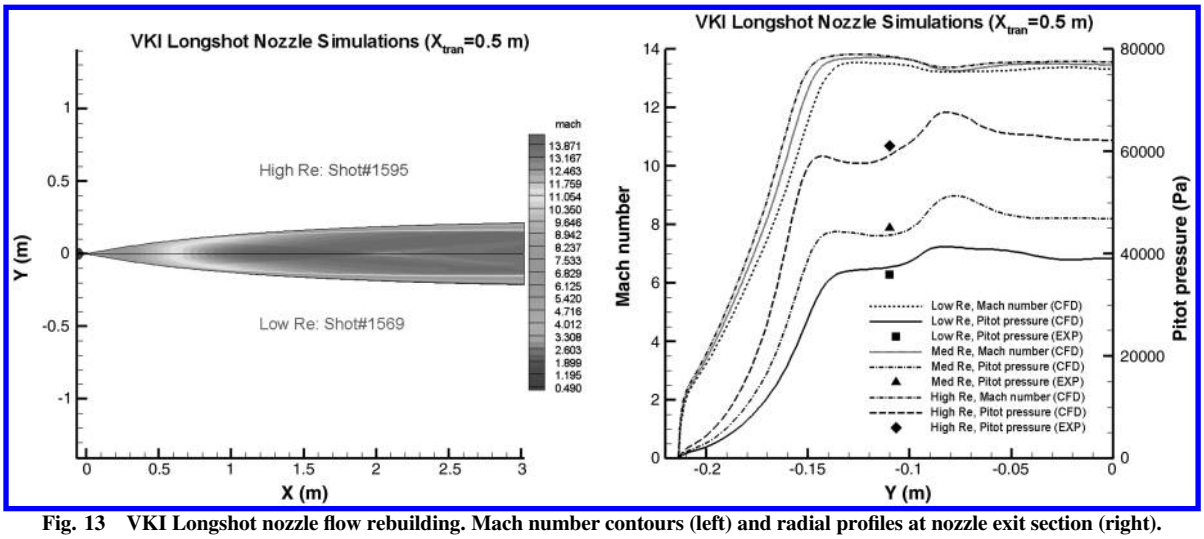

Fig. 13 VKI Longshot nozzle flow rebuilding. Mach number contours (left) and radial profiles at nozzle exit section (right).

stiff. A shock fittinglike grid adaptation (alignment of grid cells and shock surface) and a suitable distribution of points (sufficient number and regular spacing) within the shock layer in addition to the specific numerical treatment [9] has been necessary in order to overcome the numerical oscillations around the nose (i.e., the well known "carbuncle" phenomenon). The transition from laminar-to-turbulent boundary layer regime has been imposed at flap hinge line, while surface radiative equilibrium (with emissivity coefficient equal to $\varepsilon = 0.80$) has been considered for in-flight simulations.

C. Computational Fluid Dynamics Rebuilding Activities

First point of the CFD rebuilding activities of the VKI Longshot test campaign has regarded nozzle flow reconstructions, in particular the low, medium and high Reynolds number conditions of Table 4, the goal being to give a more complete characterization of the test chamber flow by combining available measurements and CFD nozzle flow simulations. Axisymmetric computations were performed by using H3NS on a 220×100 grid (with an extension including the position of the reference probe), and employing the Baldwin–Lomax algebraic eddy viscosity model when assuming a turbulent boundary layer inside the nozzle. Vibration of nitrogen was also modeled as described in Sec. IV.A, and laminar-to-turbulence transition was imposed 0.5 m downstream of the nozzle throat.

Computed results are reported in Fig. 13 in terms of Mach number contours for low- and high-Reynolds-number conditions, and in terms of radial profiles of Mach number and pitot pressure at the section where the reference probe is located (20 mm from the nozzle exit section). A test chamber core flow of nearly 0.3 m is predicted for all the conditions, and a good agreement between measured and predicted pitot pressures is found. The radial variation of predicted pitot pressure is due to the weak compression originating at the nozzle wall, and due to the change of slope typical of a contoured nozzle, that reflects on the nozzle centerline and crosses the nozzle exit section. Moreover, it has been found that the flow is vibrationally frozen downstream of the nozzle throat.

Data for test chamber flow assessment are reported in Table 6, showing a good agreement between CFD nozzle flow rebuilding results and experimental measurements of pitot pressure P_{sp}, and between predicted results and values theoretically derived of Mach number and temperature. These small percentage discrepancies (5/6% for Mach number, 3/4% for pitot pressure and 2% for static temperature) are a proof of the suitability of test chamber conditions reported in Table 4 for the IXV model flow reconstructions.

For what concerns the numerical rebuilding of the VKI Longshot experimental test campaign on the IXV model, a test matrix of ten CFD runs (Table 7) has been performed in order to cross-validate the results and confirm, also from the theoretical point of view, the different effects investigated. Ideal gas hypothesis has been made for VKI Longshot test gas. The identification of each CFD simulation with available experimental runs is also reported in the table for a proper comparison between measurements and predicted results. Note that NT and FT in the table stand for, respectively, "natural transition" and "forced transition."

The computational grid around the IXV C-model has been obtained by the flight configuration by simply scaling down the spatial coordinates (scale 1:22, $L = 0.2$ m), and properly adapting the wall stretching to Reynolds number requirements (cell dimension $= 10^{-5}$ m. at wall). A fixed wall (ambient) temperature (300 K) has been assumed for the IXV model surface. Some CFD results are reported in the following figures (Figs. 14–16), while in

Table 6 Test chamber flow assessment

	M_∞		P_{sp}, Pa		T_∞, K	
ID	Table 4	CFD	EXP	CFD	Table 4	CFD
Low *Re*	13.98	13.31	35,912.5	37,405.0	43.69	44.70
Medium *Re*	14.18	13.45	45,036.7	43,611.1	38.35	39.21
High *Re*	14.39	13.55	61,074.1	59,228.6	38.56	39.39

Table 7 VKI WT conditions CFD test matrix

No.	M_∞	Re_∞, FT/NT	Configuration	α, deg	β, deg	δ_e, deg	δ_a, deg	Flow regime	Shot no.
WT01	13.98	Low NT	Half-body/symmetric	45	0	5	0	Laminar	1569
WT02	14.05	Low NT	Half-body/symmetric	45	0	10	0	Laminar	1570/1574
WT03	14.14	Low NT	Full-body/symmetric	45	8	10	0	Laminar	1593
WT04	14.18	Medium NT	Half-body/symmetric	35	0	10	0	Laminar	1592
WT05	14.2	Low NT	Half-body/symmetric	50	0	10	0	Trans. HL	1591
WT06	14.07	Low NT	Half-body/symmetric	45	0	15	0	Trans. HL	1572/1573/1576
WT07	14.16	Low FT	Half-body/symmetric	45	0	5	0	Turbulent	1600
WT08	13.95	Low FT	Half-body/symmetric	45	0	10	0	Turbulent	1599/1603
WT09	13.98	Low FT	Half-body/symmetric	45	0	15	0	Turbulent	1602
WT10	14.39	High FT	Half-body/symmetric	45	0	20	0	Turbulent	1595

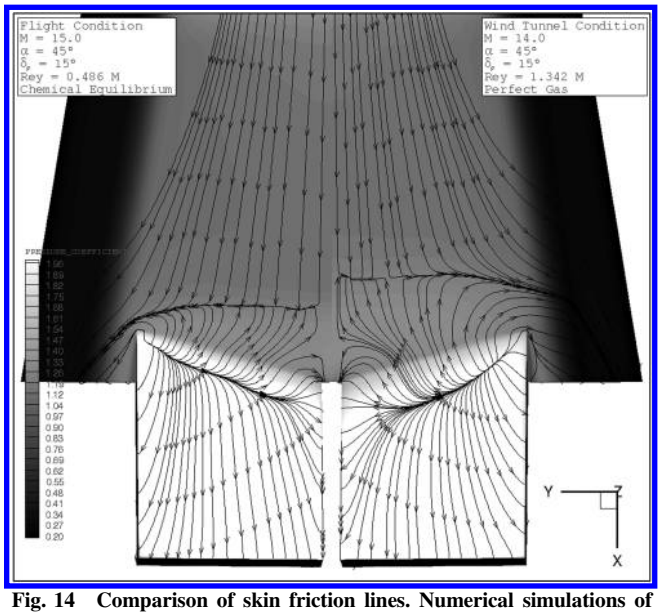

Fig. 14 Comparison of skin friction lines. Numerical simulations of conditions for flight (left) and WT (right).

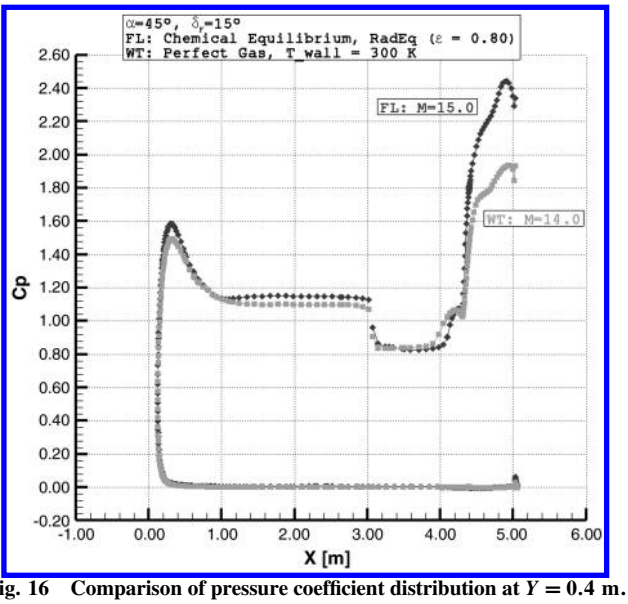

Fig. 16 Comparison of pressure coefficient distribution at $Y = 0.4$ m. Numerical simulations of flight and WT conditions.

the next section an extended comparison between numerical and experimental measurements is given.

One aim of the WT test campaign is the capability to reproduce the in-flight reentry conditions. So in order to verify this a comparison between an in-flight condition simulation ($M_\infty = 15$, $Re_{\infty,L} = 4.86 \cdot 10^5$) and one in WT condition simulation ($M_\infty = 14$, $Re_{\infty,L} = 1.34 \cdot 10^6$) is reported in Figs. 14–16, respectively, in terms of skin friction lines pattern around the flap, and heat flux and pressure coefficient longitudinal distributions at section $Y = 0.4$ m. What we want to show is the reproducibility of in-flight conditions phenomenology mainly from a qualitative point of view and in particular the general trend on pressure and heat flux distribution and the separation bubble around the flap hinge line. Note that throughout all the paper results are presented in full vehicle dimensions, i.e., experimental measurements (and their CFD rebuilding) are plotted with respect to the full vehicle reference frame. For both simulations $\alpha = 45$ deg, $\beta = 0$ deg and $\delta_{\text{flap}} = 15$ deg, while laminar-to-turbulence transition has been imposed at flap hinge line. The reproducibility of flight conditions seems to be qualitatively good, both in terms of flow features and surface properties: a similar separation bubble can be observed in Fig. 14, the larger pattern of WT case being due to a combined effect, on the transitional shock-wave boundary-layer interaction, of ideal gas hypothesis (with respect to the equilibrium gas assumption in-flight) and greater Reynolds number. The higher value of heat flux in WT conditions (see Fig. 15) is due to both fixed wall temperature hypothesis with respect to the radiative equilibrium assumed in-flight and to the different gas flow hypothesis, while the higher value of flight pressure coefficient (see Fig. 16) is due to a closer location of the bow shock (chemical equilibrium against ideal gas modeling).

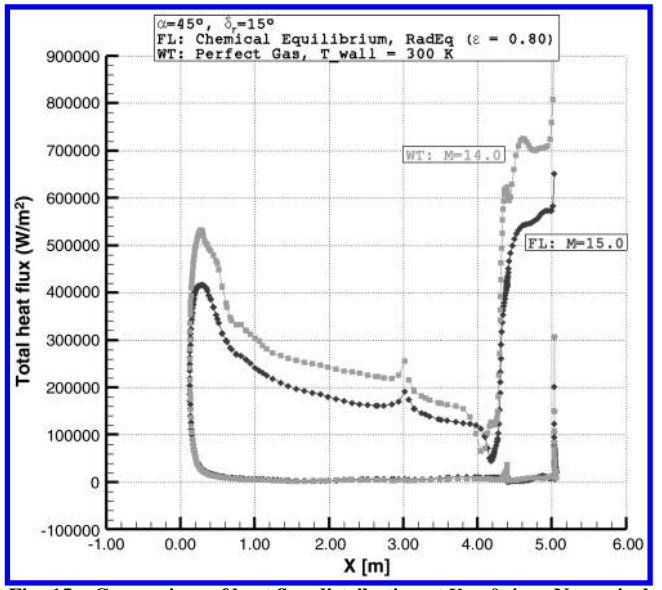

Fig. 15 Comparison of heat flux distribution at $Y = 0.4$ m. Numerical simulations of flight and WT conditions.

V. Analysis of Results

A. Experimental Results

Thirty tests were performed in VKI Longshot hypersonic WT test campaign. Angle of attack (range: 35 to 50 deg), sideslip angle (range: 0 to ±8 deg), flap-deflection angle (range: 5 to 20 deg) and Reynolds number were varied, and heat flux and pressure distributions were investigated, with a particular focus on the study of the body-flap region.

The nature of the flow is mainly driven by the Reynolds number. For low-Reynolds number the flow remains laminar. For high-Reynolds-number transition occurs towards the rear part of the body, while for medium Reynolds number a transitional flow is observed for 45 deg incidence, and a laminar flow for 35 deg incidence. At reattachment over the flap, laminar flow was obtained only in case of low-Reynolds number with flap deflection at 5 or 10 deg, and an angle of attack lower than or equal to 45 deg.

The nose region is very critical and has to support very high heat load, but in this case much higher values are reached on the flap. In the nose region the normalized heat flux (defined as q/q_{sp}, where q is the measured Heat Flux and q_{sp} is the stagnation heat flux measured at the stagnation probe, corrected by the effective nose radius factor depending on the angle of attack, i.e., the correction factor is $(R_{\text{probe}}/R_{\text{eff}})^{0.5}$; $R_{\text{probe}} = \text{const}$, $R_{\text{eff}} = R_{\text{eff}}(\alpha)$) can reach almost 1.4,

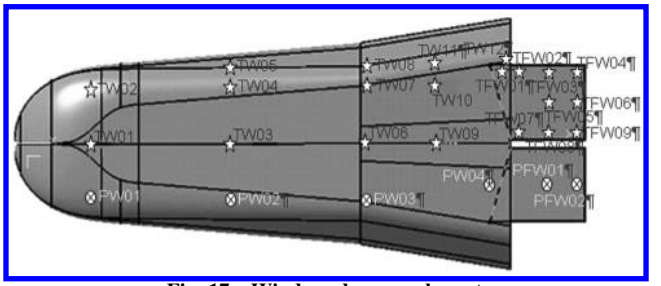

Fig. 17 Windward sensors layout.

Table 8 IXV sensors selected for EXP/CFD comparison

Body region	Spanwise location	Sensor name
	Heat flux sensors	
SYMM	$Y = 0.000$ mm	TN02-TN01-TW01-TW03-TW06-TW09
STRT1	$Y = -496.23$ mm	TW02-TW04-TW07-TW10
FLAPT2	$Y = -371.25$ mm	TFW05-TFW06-TFL01
	Pressure sensors	
STRP	$Y = +496.23$ mm	PW01-PW02-PW03
FLAPP	$Y = +371.25$ mm	PW04-PFW01-PFW02

and on the flap we can obtain values higher than 2 and up to 2.8 when a sideslip angle is applied. The critical area is the external corner close to the hinge line (TFW01; see Fig. 17). The heat flux measured close to the flap experiences similar load. This region was not massively instrumented and it seems realistic to think that the heat flux can be locally slightly higher.

The pressure coefficient distribution over the body and the flap was also investigated. We have an expected maximum value at stagnation point ($C_p \cong 1.8$), and another maximum on the flap which can reach almost 2.5.

Critical areas of the model are the nose and the flap region. The flow topology in the nose region is pretty well known, but around the flap the flow structure is more complex. There is a shock-wave boundary-layer interaction, a shock–shock interaction with a jet impinging on the flap in some cases (i.e., higher flap deflections), and strong vortices appearing around the flap. The presence of all these complex flow features makes the flow difficult to be predicted.

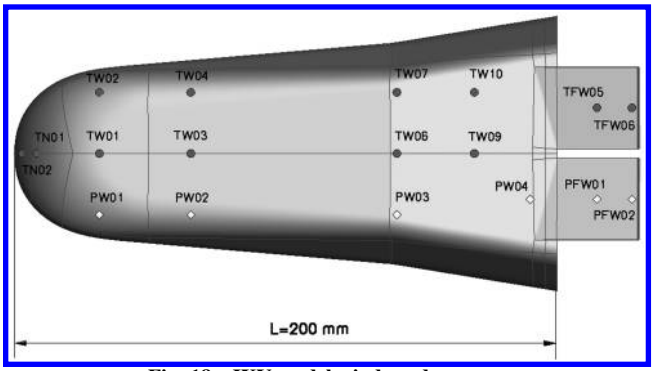

Fig. 18 IXV model windward sensors.

B. Experimental/Numerical Comparison

To meaningfully compare numerical results and experimental measurements, only for some significant conditions of Table 7, several pressure and heat flux sensors on the IXV model windward (see Table 8) have been selected as shown in Fig. 18, and the correspondent numerical slices have been extracted from CFD simulations.

A good agreement in terms of external flow structure, i.e., bow shock, shock layer, expansion at the junction on windward side, shock-wave boundary-layer interaction in the flap area and multiple-shock interaction above the flap can appreciated from Fig. 19 where a schlieren picture and the corresponding CFD visualization are reported for the $M = 14.0$, $a = 45$ deg, $de = 15$ deg conditions (see run WT06 of Table 7). Only a small difference can be remarked for the shock impingement on the flap, that results a little bit upstream in the experiment.

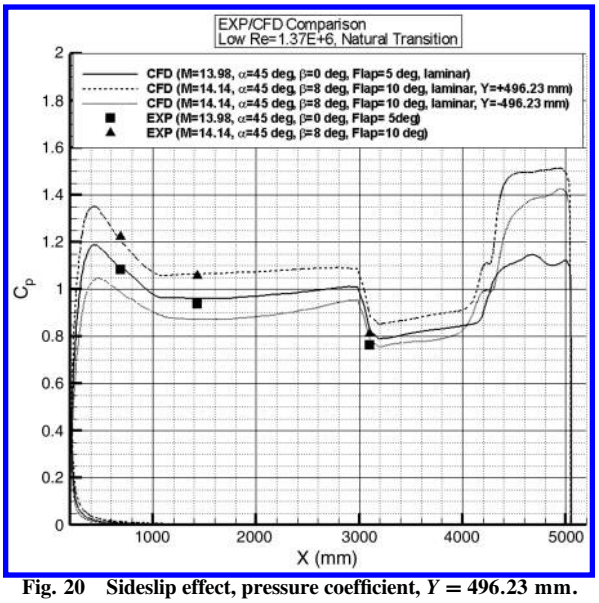

Fig. 20 Sideslip effect, pressure coefficient, $Y = 496.23$ mm.

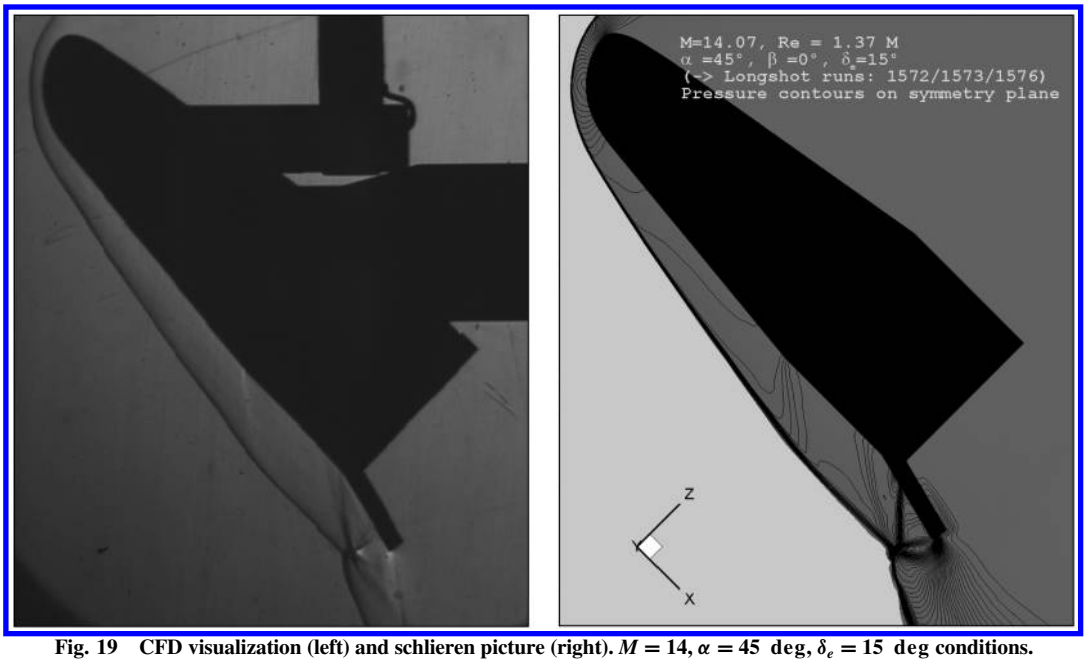

Fig. 19 CFD visualization (left) and schlieren picture (right). $M = 14$, $\alpha = 45$ deg, $\delta_e = 15$ deg conditions.

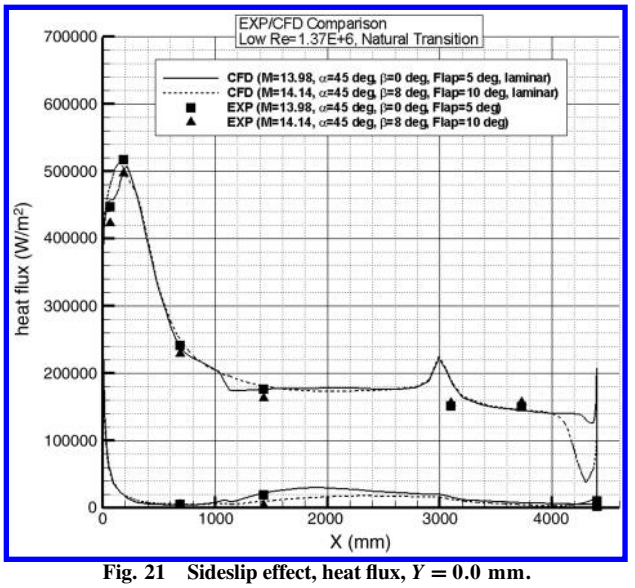

Fig. 21 Sideslip effect, heat flux, $Y = 0.0$ mm.

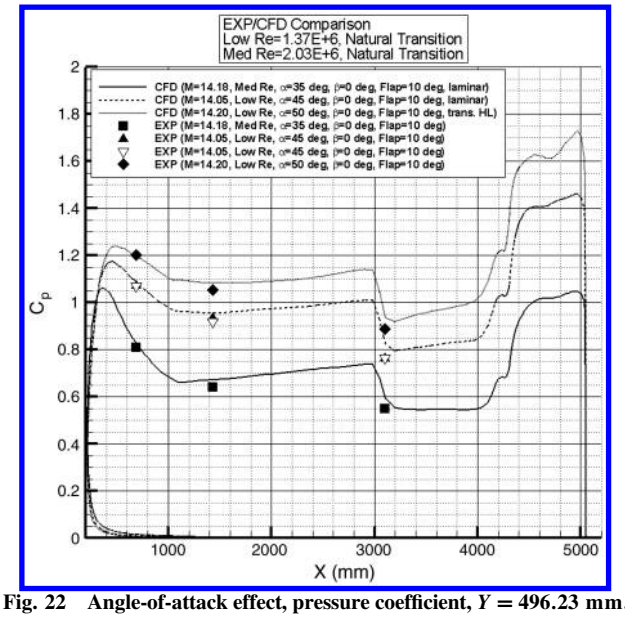

Fig. 22 Angle-of-attack effect, pressure coefficient, $Y = 496.23$ mm.

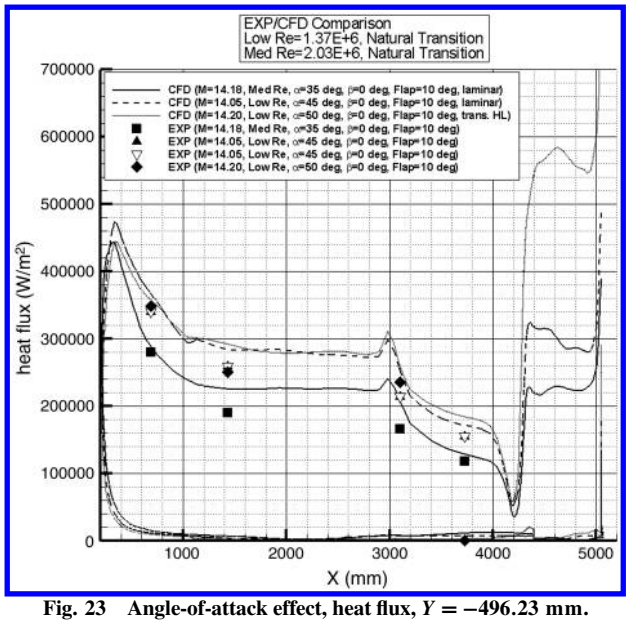

Fig. 23 Angle-of-attack effect, heat flux, $Y = -496.23$ mm.

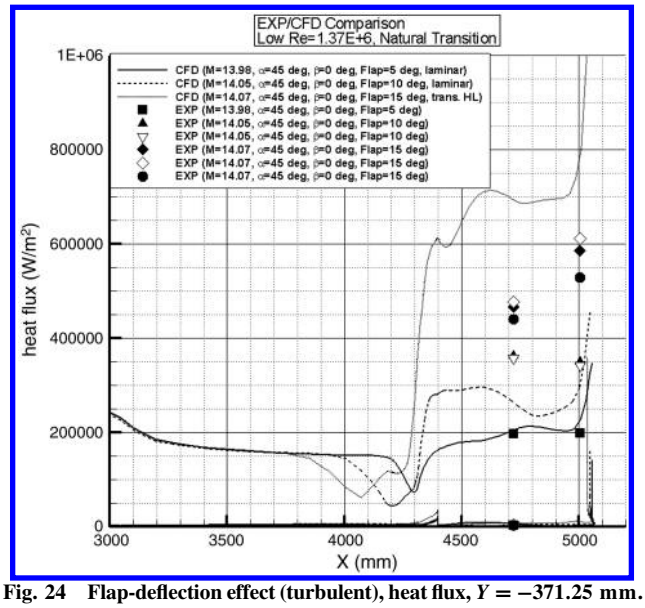

Fig. 24 Flap-deflection effect (turbulent), heat flux, $Y = -371.25$ mm.

On the windward side, sideslip effects are correctly reproduced by CFD in terms of pressure and heat flux (both at symmetry plane and $Y = -496.23$ mm) as can be seen from Figs. 20 and 21. Angle-of-attack effects are correctly reproduced by CFD in terms of pressure coefficient (Fig. 22) and slightly overestimated in terms of heat flux (Fig. 23), especially at $x = 1.5$ m station where the overprediction is about 20% and is probably due to a still transition from laminar-to-turbulent flow regime. Note that the figures, as already said, are plotted in full vehicle dimensions (length from nose to base equal to 4.4 m, length from nose to the end of not deflected flap equal to about 5.06 m).

On the body flap, angle-of-attack and flap-deflection effects are quite correctly reproduced in terms of pressure coefficient. One can only remarks a slight difference at the impingement of the jet at the end of the windward flat zone ($x = 4.2$ m) similar to what occurs at $x = 3.0$ m (Fig. 26), while laminar simulations underestimate flap heat fluxes and hinge-line transitional simulations overestimate them (see Fig. 24).

As a general comment, heat flux measured levels indicate that transition tripping devices (forced transition runs) seem to not cause a full laminar-to-turbulence transition (see Figs. 24 and 25) despite the tripping device was set to much higher height than the one predicted

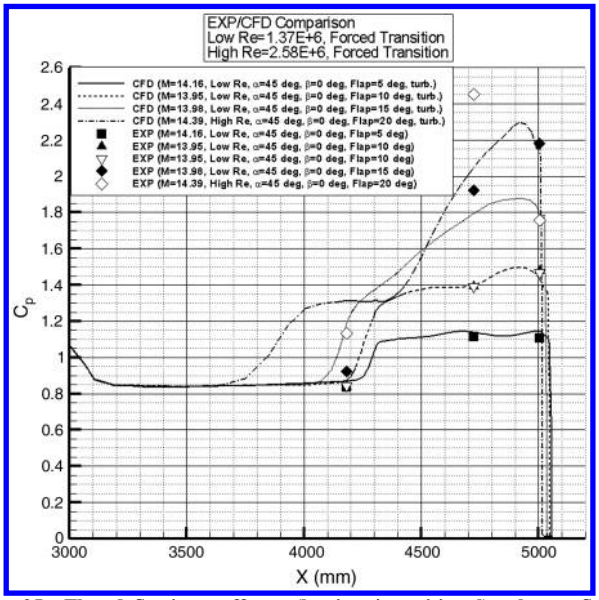

Fig. 25 Flap-deflection effect (laminar/transitional), heat flux, $Y = -371.25$ mm.

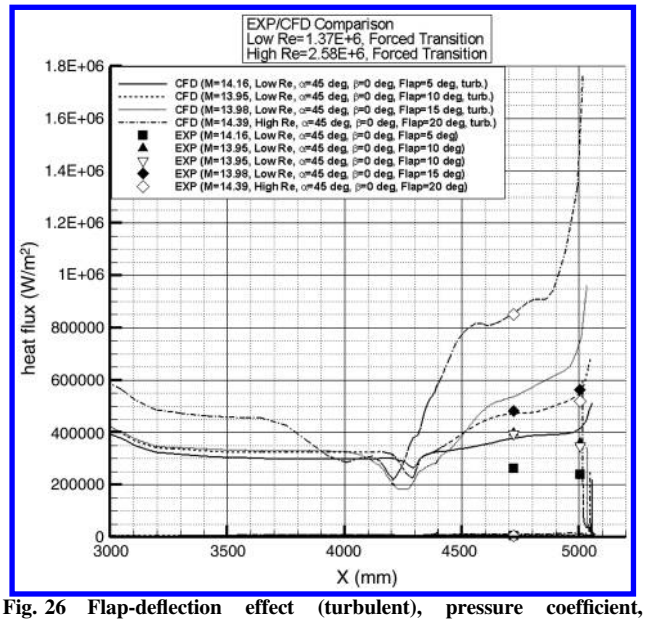

Fig. 26 Flap-deflection effect (turbulent), pressure coefficient, $Y = 371.25$ mm.

by transition Reshotko criterion (see Fig. 6), and the comparison of laminar and turbulent CFD heat flux distributions indicates a strong effect of turbulent flowfield regime not so evident in experimental measurements.

VI. Conclusions

This work has reported the main results of the aerothermodynamic hypersonic characterization of IXV, conducted by means of both CFD simulations (CIRA) and WT measurements (VKI Longshot).

WT numerical simulations indicate that the reproducibility of flight conditions in VKI Longshot test campaign is qualitatively good, both in terms of flow features and surface properties. First comparisons between experimental findings and computed results indicate a good agreement in terms of external flow structure, i.e., bow shock, shock layer, shock-wave boundary-layer interaction in the flap area and multiple-shock interaction above the flap and bubble recirculation zone over the body near the flap hinge line. Pressure coefficient and heat flux distributions obtained by means CFD show a good trend versus both the angle of attack and the angle of sideslip and the comparisons with the experimental data exhibit a general agreement except specific points over the body where the data sensors should have experienced some problems.

In general, heat flux measured levels indicate that tripping devices (forced transition runs) seem to not cause a full laminar-to-turbulence transition apart from the high Reynolds number condition, and only in the 20 deg deflected flap region. Angle-of-attack and flap-deflection effects are quite correctly reproduced on the flap in terms of pressure, while laminar simulations underestimate flap heat fluxes and hinge-line transitional simulations overestimate them.

Acknowledgments

The authors are grateful to Alexander Wagner of von Kármán Institute for his support to the experimental activities and to Paolo Binetti of Next Generation Launcher Prime for his precious collaboration during the preparation of the present work.

References

[1] Baiocco, P., Guedron, S., Plotard, P., and Moulin, J., "The Pre-X Atmospheric Re-Entry Experimental Lifting Body: Program Status and System Synthesis," 57th International Astronautical Congress, Valencia, Spain, International Astronautical Congress Paper 06-D2.P.2.02, 2006.

[2] Tumino, G., and Gerard, Y., "Europe Among the World Players in Atmospheric Reentry," ESA Bulletin 128, Nov. 2006.

[3] Oswald, J., Lüdeke, H., Longo, J., Thivet, F., Hylkema, J., Spel, M., and Dieudonné, W., "DLR-ONERA Accurate CFD Support to the Pre-X Project," Sixth International Symposium on Launchers Technologies, Munich, ONERA TP2005-232, 2005.

[4] Pandolfi, M., and Borrelli, S., "An Upwind Formulation for the Numerical Prediction of Non Equilibrium Hypersonic Flows," *Lecture Notes in Physics*, Vol. 371, 1990, pp. 416–420. doi:10.1007/3-540-53619-1_227

[5] Roncioni, P., Rufolo, G. C., Marini, M., and Borrelli, S., "CFD Rebuilding of USV-DTFT1 Vehicle In-Flight Experiment," *Acta Astronautica*, Vol. 66, 2010, pp. 1201–1219. doi:10.1016/j.actaastro.2009.10.015

[6] Grasso, F., and Falconi, D., "Shock-Wave/Turbulent Boundary-Layer Interactions in Nonequilibrium Flows," *AIAA Journal*, Vol. 39, No. 11, Nov. 2001, pp. 2131–2140. doi:10.2514/2.1209

[7] Reshotko, E., and Tumin, A., "Role of Transient Growth in Roughness-Induced Transition," *AIAA Journal*, Vol. 42, No. 4, 2004, pp. 766–770. doi:10.2514/1.9558

[8] Reshotko, E., and Tumin, A., "Investigation of the Role of Transient Growth in Roughness-Induced Transition," 32nd AIAA Fluid Dynamics Meeting, St. Louis, MO, AIAA Paper 2002-2850, 2002.

[9] Reshotko, E., "Is Re_θ/M_e a Meaningful Transition Criterion?" 45th AIAA Aerospace Sciences Meeting and Exhibit, Reno, NV, AIAA Paper 2007-943, 2007.

[10] Srinivasan, S., Tannehill, J. C., and Weilmuenster, K. J., "Simplified Curve Fits for the Thermodynamic Properties of Equilibrium Air," NASA RF 1181, 1987.

[11] Srinivasan, S., Tannehill, J. C., and Weilmuenster, K. J., "Simplified Curve Fits for the Transport Properties of Equilibrium Air," NASA CR 178411, 1987.

[12] Millikan, R. C., and White, D. R., "Systematic of Vibrational Relaxation," *Journal of Chemical Physics*, Vol. 39, No. 12, 1963, pp. 3209–3213. doi:10.1063/1.1734182

[13] Park, C., "Validation of Multi-Temperature Nozzle Flow Code NOZNT," AIAA Paper 93-2862, 1993.

T. Lin
Associate Editor